Multi-spot ultrafast laser ablation at ambient pressure – a new window on coalescing shock wave interactions

Tong Zhou[1,2], Sebastian Kraft[3], Zheng Fang[2], Walter Perrie[2*], Matthew Bilton[4], Jörg Schille[3], Udo Löschner[3], Sam E Rigby[5,6], Stuart Edwardson[2] and Geoff Dearden[2]

[1] College of Science, Jiangsu University of Science and Technology, Zhenjiang, 212100, China

[2] Laser Group, Department of Engineering, University of Liverpool, Brownlow Street, Liverpool, L69 3GH, UK

[3] Laserinstitut Hochschule Mittweida, University of Applied Sciences Mittweida, Technikumplatz 17, 09648 Mittweida, Germany

[4] SEM Shared Research Facility, University of Liverpool, Brownlow Street, Liverpool, L69 3GH, UK

[5] Department of Civil & Structural Engineering, University of Sheffield, Sheffield, UK

[6] Arup Resilience, Security & Risk, 3 Piccadilly Pl, Manchester M1 3BN, UK

*wpfemto1@liv.ac.uk

Abstract

During ultrafast laser ablation at ambient pressure, redeposition of nano-particulates occurs through backwards flux towards the end of the ablation process and is often viewed as undesirable. Here, on the contrary, we report on unique, highly symmetric redeposition patterns observed during ultrafast laser ablation of metals with closely spaced multi-spots in ambient gases. Spot symmetries were altered with a Spatial Light Modulator or beam splitting optics. At low fluence (relative to material ablation threshold), debris is highly confined within the spot patterns, while at higher fluence, jets of debris emanate along axes of symmetry reaching distances far exceeding the spot separations. These phenomena appear universal but depend on the spot proximity, substrate, ambient gas density and pulse energy. The jets, formed at the collision planes between plasma plumes, consist of agglomerated nanoparticle debris, lifted and accelerated by colliding supersonic Mach shocks whose early interactions are imprinted on the debris fields. Numerical simulation using computational fluid dynamics (CFD) of multi-spot ablation in ambient gas supports this view of the phenomena. These observations are relevant to an improved understanding of coalescing shock waves, induced air flows and re-deposition at ambient pressure.

1. Introduction

Ultrafast laser ablation at ambient pressure is complex, involving processes over a remarkably wide timescale from femtoseconds to microseconds. In metals, light absorption heats electrons rapidly so creating a high nonequilibrium state with transient electron temperature $T_e > 10^4$ K[1]. Electron-phonon coupling then heats the lattice well above the critical temperature on a picosecond timescale resulting in a fast solid-vapour/plasma transition with superheated material in a metastable state, leading to phase explosion[2]. On a nanosecond timescale, the expanding high-temperature plasma ($T_e \sim 1$ eV) with a longitudinal velocity exceeding a few km/sec creates a supersonic shock (blast) wave through energetic collisions with background gas molecules accompanied by intense plasma spectral emission[3].

While the plasma expansion in vacuo can be described as free, increasing ambient pressure alters plume geometry from spherical to cylindrical as the ambient fluid drag affects both longitudinal and radial plasma expansion[1]. Increasing pressure spatially confines the plume expansion, “aiding molecular and cluster generation with aerosols and nanoclusters generated through a nucleation-condensation process”[4] occurring towards the end of the ablation event with a vortex structure developing at the plume edge[5-7]. Nanoparticles (NPs) may also be generated directly from phase explosion or spallation during ablation[8]. On stainless steel, 90% of NPs generated by ps and fs laser pulses have diameters $\varphi \leq 100$ nm[9].

During the collision of laser-produced plasmas in vacuo, interpenetration or plasma stagnation can occur depending on atomic number Z, relative plasma velocity and plasma density[10, 11]. Significant momentum transfer takes place between the atoms/ions during stagnation. For elements with high Z (W, Mo) plasma ions tend to interpenetrate, while low Z elements (Al, C) plasma ions can stagnate. Plasma collisions in ambient air have recently been studied using Aluminium V-shaped targets where the seed plasmas collided at the mid-plane[12]. Spectrally resolved fast imaging of Al atoms along with Al^{+} and Al^{2+} ions demonstrate that "ions travel much further than neutral atoms, which are detected closer to the surface". Two high-energy, ns laser-produced Al plasmas and their shock wave interactions in ambient air demonstrated a stagnation layer behind the shock fronts at microsecond delays with gas density behind the shock front $n \sim 4.3.10^{20}$ cm^{-3} almost 20 times that of air at 1 bar pressure[13]. Even at low mBar ambient pressure, a numerical study of lateral colliding plasmas demonstrates stagnation and evidence of shock waves[14].

Debris redeposition after single spot laser ablation is a dynamic gas effect[6, 15, 16]. Backward flux redeposition during double spot, multi-pulse ultrafast laser ablation on stainless steel was recently reported by us with the appearance of aligned debris or "filaments" along the spot axis and symmetric jets emanating normal to the spot axis, fluence dependent[17]. Only a tentative explanation of the phenomena could be advanced there, connected with colliding plasmas and coalescing shock waves. In this paper, we present the first observations of debris fields during multi-spot ultrafast ablation on different metals in ambient air and Helium atmospheres with spot number $N \geq 2$. The impressive symmetry observed on various materials suggests a universal behaviour and common physical explanation which has been investigated here thoroughly and supported by simulations of coalescing shocks.

2. Materials and Methods

Experiments were performed in the Laserinstitut Hochschule Mittweida laboratory (Fig 1.): 600 fs exposure: polished samples were supported on a micro-positioning x,y,z system. The Laser beam was expanded and directed to a 50:50 beam splitter and then variable delay line (mirrors M2,M3) with tilt mirror M8 to spatially separate and temporally synchronize double spots on target. A half wave plate (HWP3) was used to bring pulse polarisations parallel. Time zero was detected through plasmonic structures when the beams were focused and overlapped spatially and temporally. The spatial distance between the pulses is monitored with a CCD camera in the focal plane. The laser system (0.6 ps/1030 nm) is a FX200-Series model, Edgewave GmbH (Wurselen, Germany) with a maximum pulse energy $E_P > 40$ μJ. The average power could be measured with a thermal detector (Gentec EO Inc., Quebec, Canada). The experiments were performed under normal conditions in air. SEM images were captured with a microscope from JOEL Ltd. (Tokyo, Japan).

Experiments were performed in the Department of Engineering, University of Liverpool (Fig 2.): 10 ps exposure: all samples were optically polished prior to laser exposure and supported on x,y,z stages (Aerotech). Laser beams were attenuated, expanded (×3) and directed to a Scanning Galvo with an f-theta lens (f = 100 mm, spot size $2\omega_0 = 22.2$ μm) after reflection from a phase-only Spatial Light Modulator (SLM, Hamamatsu, X-10468-03). The SLM was addressed with appropriate Computer-Generated Holograms (CGHs) which are generated and programmed in Labview software. A 4f optical system relayed the reflected complex optical field to the input aperture of the scanning Galvo. The laser system (10 ps/1064 nm) is a High-Q model IC355-800 with maximum pulse energy $E_P > 120$ μJ. Spot patterns and relative spot energies could be checked prior to material exposure using a pick-off mirror and focused with a long focal length lens to a Spyricon CCD camera (SP 620U). Pulse energies could be measured with a power meter/pyro-electric detector.

The pulse number is controlled by using a fast-mechanical shutter (Thorlabs SH05) which is synchronised to the SCAPS GmbH scanning software. For ablation in He, substrates were mounted in a special 3-way vacuum tight cell which is mounted on the x,y,x stage. A vacuum pump first reduced the air pressure to < 0.01 Bar after which the cell was backfilled with Helium to required pressure. Laser beams were focused on the substrate through an AR-coated window on top. A 2 lens imaging system (M ~ ×8) aligned outside the vacuum cell side window imaged the expanding plasma plumes onto the ICCD camera (Andor, iStar 734) which was synchronised by the TTL output from the Pockels Cell driver of the laser system. Scanning electron microscopy (SEM) and accompanying energy dispersive X-ray spectroscopy (EDX) was performed using a Zeiss Gemini 450 FEG-SEM equipped with an Oxford Instruments X-Max 50 mm^2 EDX detector. This was operated using an accelerating voltage between 1 – 10 kV and probe current between 500 – 1000 pA. Ansys Fluent software was used for multi-spot ablation simulations in ambient gas with the continuity equations based on the Rankine-Hugoniot equations[18]. The surface dimension was set to 2000 μm x 2000 μm with grid dimension 4 μm x 4 μm which allowed the simulations to converge.

3. Results

3.1 Femtosecond ablation

The terms “low pulse energy”, “intermediate pulse energy” and “high pulse energy” are used throughout the paper, represented by acronyms, LE_p, IE_p, and HE_p respectively. They represent LE_p = 2 μJ, IE_p = 5 μJ and $HE_p \geq 8$ μJ. while pulse exposure number lay in the range $600 \leq N \leq 1000$. Various materials (ANSI 304 Stainless Steel = SS, Copper, Silicon) were investigated using 600 fs laser two spot ablation at 1030 nm wavelength. The pulse repetition rate was kept constant at f = 5 kHz while incident spot energy Ep, fluence F, separation d and pulse number/spot N were varied.

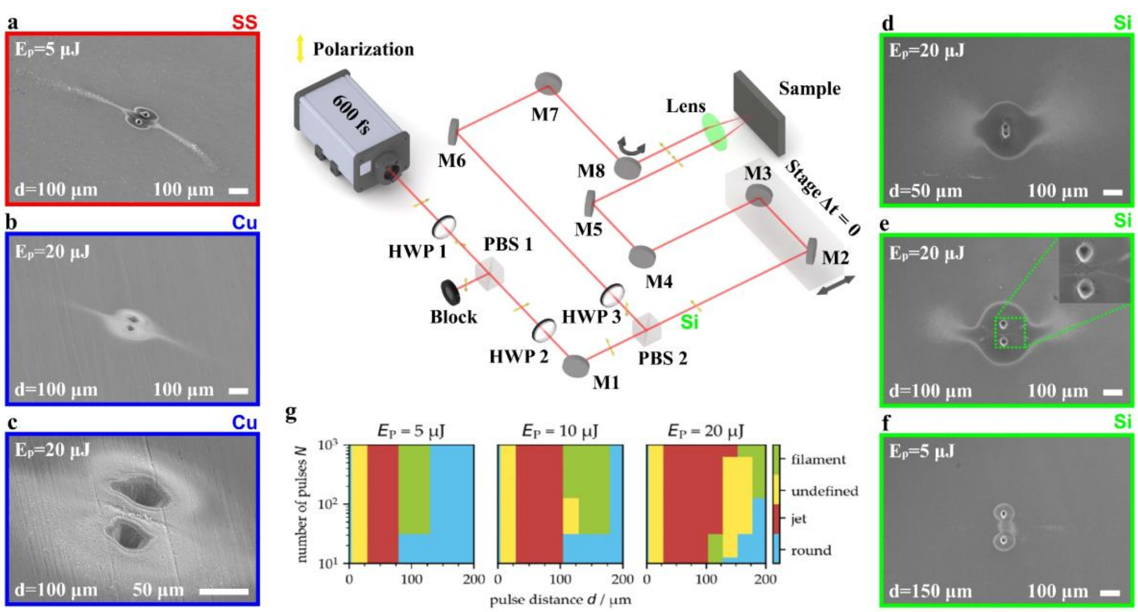

Fig. 1 SEM images of 600 fs (N = 1000) two spot ablation on SS, Cu and Si. A schematic diagram of the optical set-up for fs ablation is shown, middle top. **a** SS, IE_p = 5 μJ, d = 100 μm. Strong jets appear out to 0.5 mm from the spot centre. **b** Cu, HE_p = 20 μJ, d = 100 μm, jets here are much weaker, consistent with higher ablation threshold of Cu. **c** Cu, HE_p = 20 μJ, centre of ablation region at higher magnification of Fig. 1b, showing debris removal between spots during plume collisions. **d** Si, HE_p = 20 μJ, d = 50 μm, highly diverging debris jets are evident. **e** Si, HE_p = 20 μJ, d = 100 μm, lower divergence jets appear. **f** Si, IE_P = 5μJ, d = 150 μm, debris is now concentrated in a “filament” between the spots. **g** schematic summary of two spots stainless steel ablation with pulse energy, pulse number and spot separation (pulse distance d), demonstrating that filaments and jets are a universal feature.

Fig. 1a-f show SEM images of simultaneous two spot ablation and redeposition patterns observed in ambient air with stainless steel, Copper and Silicon. For these images, we use red edged rectangles for s. steel, blue for Cu and green for Si substrate. Spot separation d was varied in the range 50 ≤ d ≤ 150 μm with pulse exposure N = 1000. In Fig. 1a, on stainless steel with IE_P = 5 μJ (d = 100 μm, F = 1.5 Jcm^{-2}), strong jets appear perpendicularly aligned with respect to the spot axis reaching almost 0.5 mm from the spot axis. On Copper, with HE_P = 20 μJ (d = 100 μm, F = 5.7 Jcm^{-2}), Fig. 1b, jets also appear but are now significantly weaker compared to stainless steel. This is likely due to the fact that the ablation threshold of Copper, F_{0th}(Cu) = 0.28 Jcm^{-2} is much higher than F_{0th}(SS) = 0.09 Jcm^{-2} for stainless steel[19]. Fig. 1c shows an expanded image of the central region of Fig. 1b, exhibiting material removal at the collision plane between the ablation spots. Fig. 1d-f illustrate simultaneous double spot HE_P/IE_P ablation on Si while varying spot separation. In Fig. 1d (HE_P, d = 50 μm), highly diverging debris jets appear, while in Fig. 1e, (HE_P, d = 100 μm), the effect of increasing spot separation results in lower jet divergence with clear debris removal between spots. At d = 150 μm combined with lower energy IE_P, Fig. 1f, the debris is primarily concentrated in a filament between the spots. The schematic in Fig. 1g summarises the observations on two spot fs ablation of stainless steel when altering pulse energy/fluence, pulse exposure and spot separations. These results suggest that the appearance of filaments and jets is a universal feature, fluence and material dependent.

3.2 Picosecond laser ablation

With longer pulse length τ = 10 ps, multi-beam (N ≥ 2) ablation of ANSI 304 Stainless steel was studied in ambient air and Helium with the aid of a Spatial Light Modulator (SLM) addressed with appropriate CGHs based on Inverse Fourier Transforms (IFTs)[20]. Fig. 2 (centre) illustrates the laser and optical set-up used for more complex multi-beam ablation with the SLM. After attenuation, beam expansion (BE) and beam modulation with appropriate CGH, a 4f optical system re-images the complex field to the Galvo input aperture and focused by an f-theta lens to the substrate. For ablation under Helium, a gas cell with fused silica input and side windows was first evacuated then backfilled with He. The observed plasma emission is imaged to a fast ICCD camera. Fig. 2a-i show optical images of redeposition patterns at LE_p (E_p = 2 μJ, F = 0.9 Jcm^{-2}) and HE_p (E_p = 10 μJ, F = 4.5 Jcm^{-2}) exposure with N = 800 pulses and spot separation d = 100 μm. We use red dash boxes for ablation in air and green for ablation under He.

In Fig. 2a-c, the effect of altering spot geometry at LE_p results in clear debris confinement within the spot patterns. Fig. 2a, with 3 spots in an equilateral triangle, debris is also confined in this triangular geometry. In Fig. 2b with 4 spots in a square the confined debris field reflects this geometry closely. In Fig. 2c, with 5 spots, the centre spot now acts to further direct the backward flux to yield clear linear multiple narrow filaments. The effect of HE_p multi-beam ablation in air is shown in Fig. 2d-f, exhibiting strong debris removal (jets) along axes of symmetry. In Fig. 2d, three jets are observed, while in Fig. 2e, four jets appear, two emanating along each axis of symmetry. A rotated cross appears at the centre. In Fig. 2f, the 5 spots pattern again shows 4 diverging jets with clear debris removal in a well-defined diamond shape around the central spot. The small spots in Fig. 2d-f are ablation spots due to low-intensity ghost beams and the remaining zero order when their fluence exceeds the multi-pulse ablation threshold on stainless steel. These are expected since the CGHs are rarely perfect in modulation but full phase maps used here (Δφ = 0 - 2π) are more efficient than binary holograms[21]. However, the debris around these small spots indicates the local gas flow direction behind the shockwaves. The effect of using ambient He gas is shown in Fig. 2g-h. Fig. 2g shows 2 spot HE_p ablation under 1 Bar He where redeposition is almost absent with weak debris confinement and filaments between ghost beams and the main ablation spots. This contrasts with 2 spot ablation femtosecond in air, Fig. 1a where strong jets appear, even with intermediate energy IE_P. Fig. 2h shows 5 spot HE_P ablation in He at 2.5 Bar pressure, yielding symmetric debris confinement within the spot pattern with little redeposition. Ablation under Helium is more akin to free plasma expansion under vacuum.

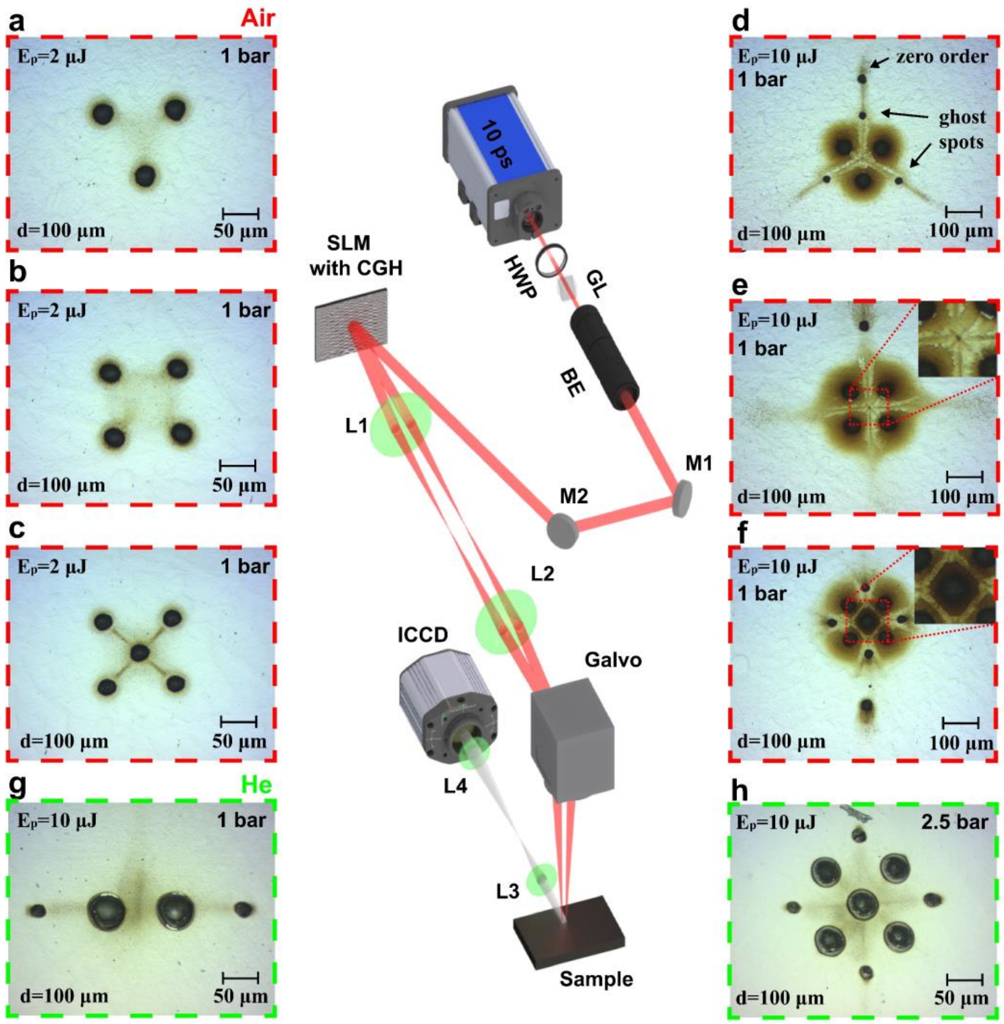

Fig. 2 Optical images of multi-spot, 10 ps laser ablation of s. steel with LE_p and HE_p under air (dashed red boxes), He (dash green boxes). Pulse exposure N = 800 pulses. A schematic of the optical set-up is shown in the centre. **a** air, LE_p = 2 μJ, 3 spot ablation in triangular pattern, debris also shows confinement in triangular geometry. **b** air, LE_p = 2 μJ, 4 spot square pattern with clear debris field, confined in this geometry. **c** air, LE_p = 2 μJ, 5 spot ablation, now resulting in linear filaments between spots. **d** air, HE_p = 10 μJ, 3 spot ablation with symmetric jets observed along axes of symmetry. **e** air, HE_P = 10 μJ, 4 spot square ablation with 2 opposing jets emanating along each axis of symmetry. **f** air, HE_p = 10 μJ, 5 spot ablation showing 4 jets with clear debris removal in a diamond shape around the central spot and high divergence shock debris removal. **g** He, 1 Bar, HE_p = 10 μJ, 2 spot ablation: redeposition is almost absent with weak debris confinement and filaments between ghost beams and the main ablation spots. **h** He, 2.5 Bar, HE_p = 10 μJ, 5 spot ablation, yielding symmetric debris confinement within the spot pattern but little redeposition.

SEM images and EDX spectra of debris from LE_P and HE_P 5 spot ablation in air at atmospheric pressure are shown in Fig. 3. In Fig. 3a, at LE_p, debris concentration between spots is clear. Fig. 3b shows the expanded region within the dotted circle of Fig. 3a and a darker region appears between the spots. The EDX elemental map of this region (right) shows a higher Oxygen Kα signal around the spot rims and between spots, inferring that the darker region is due to oxidation. At HE_P (E_p = 15 μJ, F = 6.8 Jcm^{-2}), Fig. 3c, clear jets appear along the symmetry axes while the debris field within the jet in the small, dotted circle (Fig. 3c) which is shown in Fig. 3d at higher magnification. This agglomerated nano-particulate material, with μm size dimension shows elongation along the jet axis. An enhanced Oxygen Kα signal is also detected in the EDX map of the jet material (right). Fig. 3e shows the detailed EDX elemental spectrum intensities of the region indicated in Fig. 3d, confirming a higher oxygen concentration detected in the agglomerated jet debris (spectrum 2) when compared to the underlying metal surface (spectrum 1).

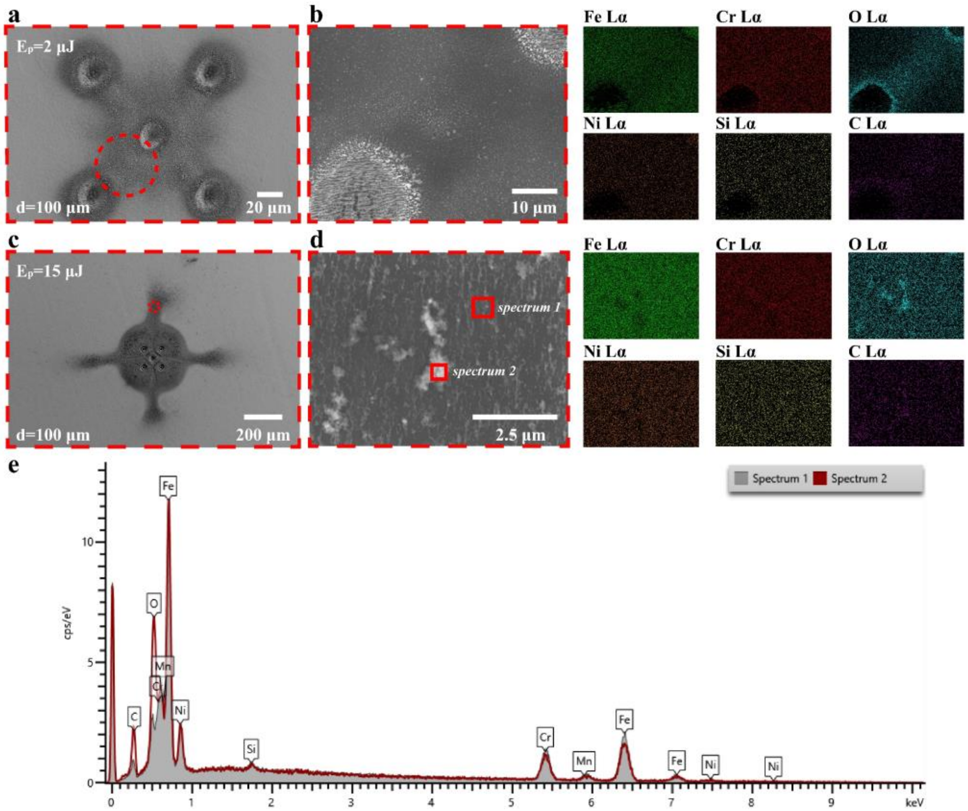

Fig. 3 SEM images and EDX spectra of debris from LE_P and HE_P 5 spot ablation in air at atmospheric pressure. **a** LE_p = 2 µJ ablation, where debris field is concentrated between and within spots. **b** LE_P = 2 µJ, expanded region within the dotted circle of Fig. 3a with a darker region directed between the spots. The EDX elemental map (right) of this region shows a higher Oxygen Kα signal around the spot rims and between spots. **c** HE_P = 15 µJ ablation, with 4 jets appearing along the symmetry axes. **d** HE_P = 15 µJ, high magnification image of jet debris within the dotted circle (Fig. 3d). This agglomerated nano-particulate material, with µm size dimension shows elongation along the jet axis. An enhanced Oxygen Kα signal is also detected in the jet material, shown in the EDX map of this region (right). **e** detailed EDX elemental spectrum intensities of the regions indicated in Fig. 3d. A higher Oxygen concentration is detected in the µm size jet nano-particle agglomerate (spectrum 2) when compared to the underlying metal surface (spectrum 1).

3.3 Plasma emission

Using a fast ICCD camera, time-resolved plasma plume emissions from HE_p = 15µJ,, picosecond multi-spot stainless steel ablation in ambient air and in He were observed, Fig. 4. Red and green dotted boxes relate to plasma expansion in air and He respectively. The Gate width was 5 ns, spot separation d = 95 µm. All images were normalized to the peak intensity. In Fig. 4a, three triangular spot plasma plume collisions from stainless steel in 1 bar air occur at delay time t ≥ 15 ns while demonstrating longitudinal plasma deceleration and rapid transverse plasma plume expansion. The corresponding ablation and redeposition pattern are shown in Fig. 2d. Initial longitudinal expansion velocity can be estimated to be v ~ 3 km/s. In Fig. 4b, with 2 spot ablation under air, the plumes again show collisions after 25ns, decelerate and expand transversely. In Fig. 4c, under low density He at ambient pressure (ρ_0 = 0.16 kg/m^3), fast longitudinal plasma expansion at speed v ~ 6 km/s is observed with plumes colliding within 15 ns. They leave the surface, reminiscent of free plasma expansion in a vacuum.

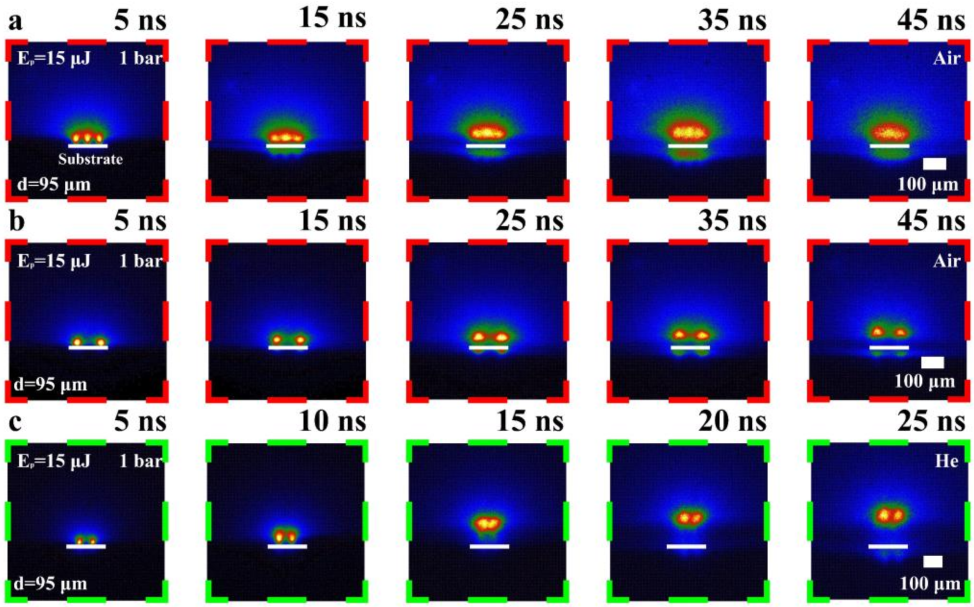

Fig. 4 Time-resolved plume emission on ICCD with HE_p = 15μJ, multi-spot (d = 95 μm) ablation of stainless steel in air and He at 1Bar pressure. **a** air, 3 triangular spots, plasma plume collisions occur at delay time t ≥ 15 ns while demonstrating longitudinal plasma deceleration and rapid transverse plasma plume expansion. Initial longitudinal expansion velocity can be estimated to be v ~ 3 km/s. **b** Two spot in air: seed plasmas collide by 25ns delay, decelerate and show radial plume expansion. **c** He, two spot, where, due to its low density (ρ_0 = 0.16 kg/m^3), fast longitudinal plasma expansion at speed v ~ 6 km/s is observed with plumes colliding within 15 ns. They leave the surface, reminiscent of free plasma expansion in a vacuum.

4. Theory: Simulation of coalescing shock waves in air

To investigate whether laser-induced shockwave interactions influence the debris patterns, the temporal pressure evolution following multi-spot ablation in the ambient atmosphere was simulated using Ansys Fluent (CFD) software. The 2D pressure field changes are solved by Euler equations of gas dynamics (conservation of mass, energy and momentum) using the implicit method. The details of plasma physics are neglected in the simulation with initial condition of the laser-induced micro-blasts considered as point sources[22]. The air environment is assumed to be a perfect gas, and the boundary conditions are set as non-reflecting. The resulting pressure change could be calculated by setting the initial conditions following the Sedov-Taylor model[22-24] where the position of the shock wave propagation in air R(t), the maximum pressure P(R), speed U and temperature T behind the shock front is given by,

$$\mathrm{R(t)} = \left(\frac{E_s}{\rho_0 K}\right)^{\frac{1}{5}} t^{\frac{2}{5}} \tag{1}$$

$$P(R) = 0.155\frac{Es}{R^3} \tag{2}$$

$$U = 0.360R^{-\frac{3}{2}}\left(\frac{Es}{\rho_0}\right)^{\frac{1}{2}} \tag{3}$$

$$T = \frac{2\gamma}{(\gamma+1)}\left[\frac{(\gamma-1)}{(\gamma+1)}M^2 + 1\right]T_0 \tag{4}$$

where E_s is the energy released, ρ_0 is the density of the air, K is a dimensionless constant which depends on the heat capacity ratio γ, and M is the shock Mach number, $M = \frac{U}{v_{sound}}$. For air at atmospheric pressure and room temperature, ρ_0 = 1.274 kg/m^3, γ = 1.4, $v_{sound} = 344\ \mathrm{m}/s$ and K = 0.856.

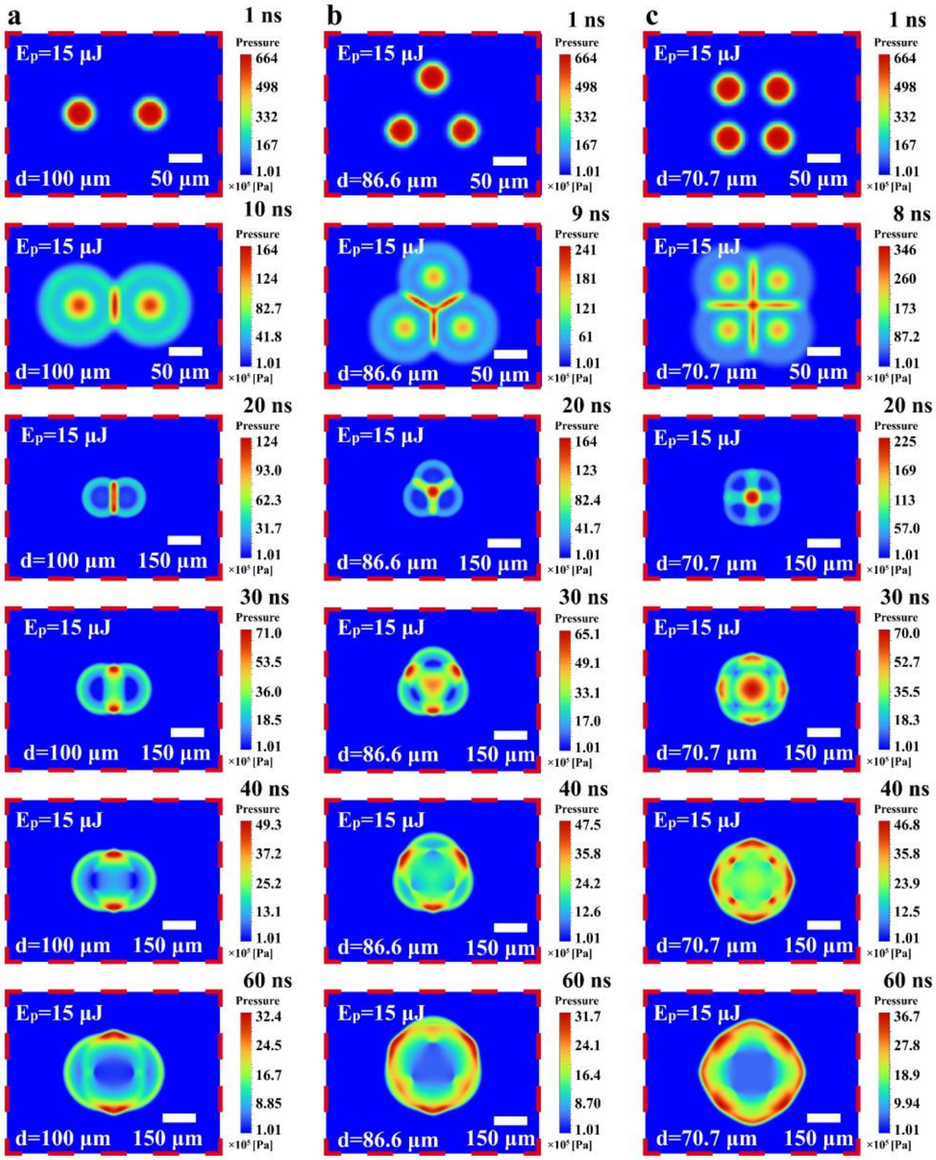

Fig. 5 Simulation of multi-spot HE ablation on stainless steel in air, E_P = 15 μJ, delay times 1- 60 ns. **a** 2 spot, d = 100 μm: coalescing shocks appears between the two spots after a 20ns delay with a pressure gradient directed along the jet axis, evident after 30 ns. By 60ns delay, a diverging Mach shock appears with the central region now back to ambient pressure. **b** 3 spot triangular, d = 86.6 μm: shocks appear by 9 ns delay and the coalescence of the three shocks is apparent at the geometric centre by 20 ns. Expansion continues along the symmetry axes with maximum pressures at the interacting shock fronts which diverge by 60 ns delay. **c** 4 spot, d = 70.7 μm : the pressure field maxima display a square symmetry along the axes at 8 ns delay and coalescing shocks again produce a pressure maximum at the geometrical centre by 20 ns delay with shock fields expanding along the two symmetry axes. By 40 ns delay, the interacting and diverging shock fronts are apparent.

During ablation, the energy released in the plume is significantly lower than the incident pulse energy E_p[25]. We have estimated the conversion efficiency by measuring the ablation rate/pulse and the plume kinetic energy (KE). From the plasma temperature T_e ~ 1 eV [17], we estimate that all Fe atoms are initially ionized to Fe^{+1} ions, requiring IP = 7.9 eV/atom. The major contributions to the energy balance are the evaporation enthalpy, plasma temperature and plume KE and consequently, we estimate E_s/E_p ~ 0.21. This value appears reasonable in view of the fact that plasma absorption with ultrafast pulses is almost negligible. Setting HE_P = 15 μJ (E_s/E_p ~ 0.21), plume energy with the shock wave pressure, radius and temperature at delay time Δt = 1 ns was estimated to be P = 684.4 bar at R = 19.6 μm and T_0 = 22000 K, respectively.

Results of these HE_P simulations with, 2 spot, 3 triangular spot and 4 spot in a square geometry are shown in Fig. 5a-c. In each case, the distance from spots to the geometrical centre (collision point) equals 50 μm. A symmetric temporal development of shock wave interactions on the nanosecond timescale with linear shock regions appearing between spots. In Fig. 5a, a coalescing shock appears after 10ns with overpressure (P_{max} ~ 160 Bar), a linear shock region between spots after a 20ns delay and a clear pressure gradient along the jet axis evident after 30 ns. The interaction of the two expanding shock waves creates a diverging Mach shock at a time delay of 60 ns with the central region now back to ambient pressure. In Fig. 5b, simulating three spot ablation, a triangular overpressure region appears by 10 ns delay and the coalescence of the three shocks is apparent at the geometric centre by 20 ns with 160 Bar overpressure. Expansion continues along the symmetry axes with maximum pressures at the interacting shock fronts which diverge by 40 ns delay. In Fig. 5c with four simultaneously irradiating laser spots, the pressure field displays a square symmetry at 10 ns and coalescing shocks again produce a pressure maximum at the geometrical centre by 20 ns delay with shock fields expanding along the two symmetry axes. By 30 ns delay, the interacting and diverging shock fronts are apparent. The simulations of transient pressure fields reflect the spot geometries, and observed debris removal patterns from HE_P two, three and 4 spot ablation (Fig. 1 and Fig. 2)**.**

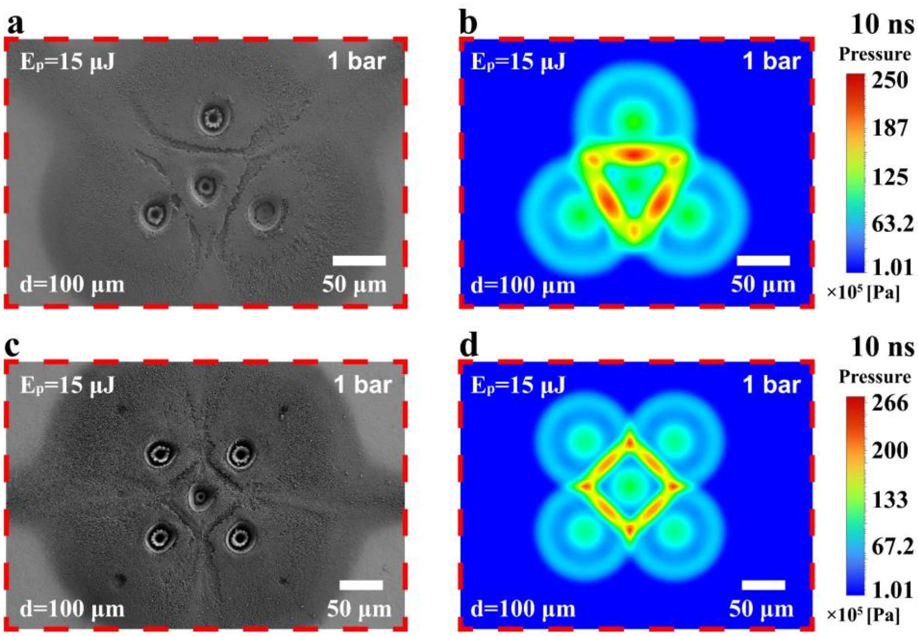

Fig. 6 SEM images of the multi-spot HE_p = 15μJ, debris field observed during ablation on stainless steel in air and corresponding CFD simulations. **a** 3+1 spot ablation showing debris removal. **b** simulation of corresponding HE_P, 3+1 pressure field at delay time Δt = 10 ns highlighting the triangular pressure field symmetry around the centre with similar dimensions. **c** HE_P, 5 spot pattern with debris field removal in a square pattern round the centre spot. **d** simulation of HE_P 5 spot pressure field at delay time Δt = 10ns which replicates this well-defined square symmetry.

Fig. 6 shows SEM images of more complex multi-spot HE_p (N = 1000) ablation of stainless steel in air and corresponding CFD simulations. Fig. 6a shows the (3+1) debris field with shockwave removal of debris in triangular geometry around the central spot. The simulation of corresponding 3+1 pressure field at delay time Δt = 10 ns is shown in Fig. 6b on the same scale with a triangular high pressure shocked region matching that in Fig. 6a. In Fig. 6c, the 5 spot ablation pattern shows debris removal in a square pattern around the centre, while in Fig. 6d, the simulation of this pressure field at delay time Δt = 10 ns replicates this well-defined square symmetry in the coalescing shocks.

Fig. 7 presents data from simulations of LE_P two spot ablation of stainless steel in ambient air. Fig. 7a shows the calculated pressure with time at the midpoint with spot separations from 50 μm ≤ d ≤ 250 μm. The time to reach maximum pressure increases with d as expected while peak overpressure falls rapidly. The insert shows an expanded scale for delay time Δt ≥ 80 ns and demonstrates that rarefaction occurs with pressure falling below 1 Bar. Fig. 7b shows the simulated 2D pressure field from LE_P, 2 spot (d =100 μm) ablation at time delay Δt = 140 ns. The two white dots mark the spot positions. There is evidence here of secondary shocks moving towards the centre. In Fig. 7c, the simulated pressure along the axes parallel (X-axis) and normal (Y-axis) to the spots (Fig. 7b) at delay time t = 140 ns is shown, where negative pressure gradients are evident along both axes. The Y-axis peak pressure is significantly higher than that parallel to the spots.

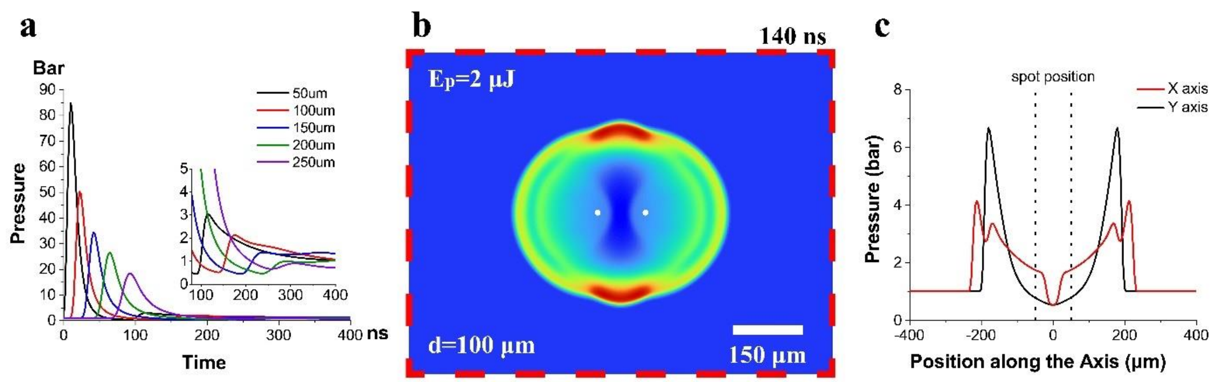

Fig. 7 a Simulated pressure with time at the centre of LE_P = 2μJ, spot ablation when varying spot separation, 50 μm ≤ d ≤ 250 μm. The insert shows an expanded scale for delay time t ≥ 80 ns. **b** simulated 2D pressure field of LE_P 2 spot ablation at time delay t = 140 ns with evidence of inward moving secondary shocks **c** simulated pressure along the axes parallel (X) and perpendicular (Y) to spot axis for Fig. 6b at delay time t = 140 ns. Note the negative pressure gradient in both directions towards the centre and rarefaction near centre. The spot positions are shown by the dotted lines.

5. Discussion

When a pulsed laser beam ablates a metal surface in an ambient atmosphere, the expanding plasma plume can be likened to a micro-detonation[24, 26]. As the plume expands supersonically, this results in a Mach shockwave and plume pressure gradient. The debris field around a circular laser spot is then spherical from symmetry. The effect of adding simultaneously generated ablation plumes alters this symmetry accordingly when the spots are in close proximity.

The study of shock waves through detonation goes back to the 1950's[24, 27] while laser-generated plume expansion into background gases indicates that the compressed background gas layer temperature behind the shock front depends on the Mach number[25]. The study of spherical and cylindrical converging shock waves and their stability has been researched extensively[27-29].

The effect of multiple ablation plumes in close proximity, creating coalescing shock waves, would be expected to increase the transient peak overpressures in certain regions. The interaction and coalescence of simultaneous, multiple blast waves from explosive detonations were studied recently through Schlieren simulations with symmetric geometries similar to those used here with multi-spot ablation[30]. The predicted pressure fields show high symmetry and pressure gradients along the axes of symmetry. Our simulations of multi-beam ablation also predict the symmetry of interacting shocks observed experimentally, strongly suggesting that supersonic shocks are involved, even though the pulse energies used here are relatively small. There is evidence in our experimental results that Mach Stems[31] also appear, Fig. 5a&c.

The interaction of quasi-stationary shockwaves during fs laser of multiple excitation spots at a water/air interface was observed by transient reflection due to supersonic colliding airflows normal to the spot axes, with shock symmetry reflecting spot geometries[32, 33]. In particular, their 4 spot reflection image (with geometry due to refractive index changes during shock wave coalescence) showed the precise shock wave pattern with a cross at centre, remarkably similar to our 4 spot re-deposition pattern, Fig.2e. In He, however, the shocks disappeared due to the low gas density, and our observations of high energy multi-spot ablation in He, also showing the absence of jets, are consistent with references [32, 33]. As the speed of sound in He, $v_S \sim 1000$ m/s, the Mach number is reduced by a factor of 3 compared to air, while the low density allows nearly free plasma expansion with speed v > 6 km/s, (Fig. 4). Our elemental analysis of the debris from stainless steel during LE_P and HE_P multi-spot ablation, investigated using EDX (Fig. 3) confirmed significantly increased levels of oxygen (O Kα signal) around spot rims, between spots and in the agglomerated nano-particulate material in the jets (Fig.3b,d). Combustion occurs during single and multi-spot ablation due to the exothermic reaction of Fe with Oxygen likely resulting in Fe_2O_3 and Fe_3O_4 debris where reaction enthalpies are 824 kJ/mol and 1118 kJ/mol respectively[34]. However, the shock wave acts as a barrier to combustion, so molecular formation probably occurs towards the end of the ablation process after shock wave collapse[4]. We estimate that oxidation adds only 10 % to the energy balance.

During surface ablation with ultrafast laser pulses (as opposed to nanosecond pulse irradiations), more stable plasma plumes are generated by avoiding melt and plasma absorption. Ablation thresholds are also much lower. This results in very fine nanoparticles and agglomerated nanoparticle debris, created in the plasma collisions with the ambient gas along with phase explosion. At low energy in ambient air, LE_p ablation rate and debris are minimised while shock wave pressures are significantly reduced, hence unable to remove surface debris. CFD simulations carried out at LE_p and HE_p demonstrated self-similar pressure field geometries but at different times scales due to the differences in the rate of shock wave expansion. We infer that long after shock waves have decayed, the following air flows due to the negative pressure gradients and rarefactions can drive NPs in the air towards the centre to create directed redeposition by backword flux. If we look at the simulations of LE_p 2, 3 and 4 spot exposure at later times, Fig. 5a-c where $\Delta t = 60$ ns, the pressure fields exhibit linear, triangular and square shaped central low pressure regions respectively. The plume NPs for 2 spot would then be directed towards the spot axis while for N > 2 these geometries experience radial negative pressure gradients, confining debris within spot geometry.

The plasma lifetimes observed here, $\tau_{pl} \leq 100$ ns << interpulse period $\tau = 200$ μs at 5 kHz pulse repetition rate, so that plasma absorption from following pulses is negligible. High energy multi-spot, multi-pulse ablation allows the build-up of sufficient debris on the substrate surface by backward flux, which, due to the agglomerated low-density nano-particulate nature, becomes a surface layer sensitive to the coalescing shock waves and gas flow fields (rarefactions) behind shocks, ejecting surface debris along axes of symmetry. The early high-pressure shock interactions imprint the shock symmetry on the debris fields, and our experimental results are supported by the simulations. A universal behaviour, independent of material has been observed with filaments and jets when allowing for the varying material ablation thresholds and ambient gas density. The observations at high energies can be regarded as a form of laser shock cleaning which is more generally accomplished with plasma breakdown in the air above a surface[35]. Dust removal from a surface has been observed behind a propagating shock wave [36]. Shock wave generated cavities at an air/water interface with fs pulses at an ultrahigh intensity $I > 10^{15}$ Wcm^{-2} have also been observed[32] while within fused silica, material densification was recently reported due to the high pressure shocked regions ($P_{max} > 10^5$ Bar) between spots[37].

Coalescing blast waves, which have been shown to obey common scaling laws [18], allow for direct read-across with larger scale high explosive and nuclear blast data. There is a potential application, therefore, for using smaller-scale, well-controlled laser ablation techniques to study the interaction of blast waves from multiple sources to mitigate the damage to complex structural forms, replicable by treating a reflecting surface as a symmetry plane and designing the experiment accordingly [38].

CFD simulations were related to multi-pulse exposure on s. steel where we estimated the conversion efficiency from incident pulse energy to expanding plasma plume to be $E_S/E_P = 0.21$. On other materials, this ratio will be different – and needs to be determined, but the experimental observations of a universal multi-spot ablation behaviour on Stainless Steel, Cu and Si with jets and filaments, material dependent, encourages us to suggest that CFD modelling may also be applied to other materials when allowing for material reflectivity, ablation threshold, and pulse to plume conversion efficiency.

6. Conclusions

Due to the capabilities of a Spatial Light Modulator, able to produce arbitrary spot patterns with uniform and non-uniform laser spot energies, the observations here open up a potentially useful new diagnostic technique for the study of coalescing shock waves and supersonic air flows using relatively low energy ultrafast laser pulses. During multi-spot ablation in ambient air at low pulse energies, debris is highly confined within the spot patterns due to converging air flows towards the end of the ablation process. On the contrary, at higher fluence, jets of debris, lifted and accelerated by colliding supersonic Mach shocks on the nanosecond timescale, emanate along every axis of symmetry. These phenomena appear universal but depend on the spot proximity, substrate and ambient gas density. This approach opens up a new window on coalescing shock waves based on observed debris re-deposition patterns which complement techniques using transient reflection[32] or fast transient absorption[19]. However, a major advantage here is that at low shock wave intensities, where refractive index changes in the air may not be visible anymore, the debris field around spots and confined within spot patterns now highlight the air flows following weak shocks.

References

1. N. Farid, S. Harilal, H. Ding, and A. Hassanein, "Dynamics of ultrafast laser plasma expansion in the presence of an ambient," Applied Physics Letters **103**, 191112 (2013).
2. N. M. Bulgakova, A. N. Panchenko, V. P. Zhukov, S. I. Kudryashov, A. Pereira, W. Marine, T. Mocek, and A. V. Bulgakov, "Impacts of ambient and ablation plasmas on short-and ultrashort-pulse laser processing of surfaces," Micromachines **5**, 1344-1372 (2014).
3. S. Harilal, N. Farid, J. Freeman, P. Diwakar, N. LaHaye, and A. Hassanein, "Background gas collisional effects on expanding fs and ns laser ablation plumes," Applied Physics A **117**, 319-326 (2014).
4. S. S. Harilal, B. E. Brumfield, B. D. Cannon, and M. C. Phillips, "Shock wave mediated plume chemistry for molecular formation in laser ablation plasmas," Analytical chemistry **88**, 2296-2302 (2016).
5. A. Pereira, P. Delaporte, M. Sentis, W. Marine, A. L. Thomann, and C. Boulmer-Leborgne, "Optical and morphological investigation of backward-deposited layer induced by laser ablation of steel in ambient air," Journal of applied physics **98**, 064902 (2005).
6. S.-B. Wen, X. Mao, R. Greif, and R. E. Russo, "Expansion of the laser ablation vapor plume into a background gas. I. Analysis," Journal of applied physics **101**, 023114 (2007).
7. S. Xu, R. Ding, C. Yao, H. Liu, Y. Wan, J. Wang, Y. Ye, and X. Yuan, "Effects of pulse durations and environments on femtosecond laser ablation of stainless steel," Applied Physics A **124**, 1-8 (2018).
8. M. Spellauge, C. Doñate-Buendía, S. Barcikowski, B. Gökce, and H. P. Huber, "Comparison of ultrashort pulse ablation of gold in air and water by time-resolved experiments," Light: Science & Applications **11**, 1-13 (2022).
9. S. Barcikowski, J. Walter, A. Hahn, J. Koch, H. Haloui, T. Herrmann, and A. Gatti, "Picosecond and femtosecond laser machining may cause health risks related to nanoparticle emission," J. Laser Micro/Nanoeng **4**, 159-164 (2009).
10. C. Fallon, P. Hayden, N. Walsh, E. Kennedy, and J. Costello, "The effect of wedge angle on the evolution of a stagnation layer in a colliding plasma experiment," in *Journal of Physics: Conference Series*(IOP Publishing2014), p. 012036.
11. C. Fallon, P. Hayden, N. Walsh, E. Kennedy, and J. Costello, "Target geometrical effects on the stagnation layer formed by colliding a pair of laser produced copper plasmas," Physics of Plasmas **22**, 093506 (2015).

12. S. Davitt, N. Walsh, T. Kelly, and J. Costello, "Colliding laser plasmas formed in air," in *Journal of Physics: Conference Series*(IOP Publishing2019), p. 012032.
13. Z. Yang, W. Wei, J. Han, J. Wu, X. Li, and S. Jia, "Experimental study of the behavior of two laser produced plasmas in air," Physics of Plasmas **22**, 073511 (2015).
14. S. K. Yadav, B. G. Patel, R. Singh, A. Das, P. K. Kaw, and A. Kumar, "Numerical study of the lateral interactions of two plasma plumes," Journal of Physics D: Applied Physics **50**, 355201 (2017).
15. S. Singh, M. Argument, Y. Tsui, and R. Fedosejevs, "Effect of ambient air pressure on debris redeposition during laser ablation of glass," Journal of applied physics **98**, 113520 (2005).
16. F. Garrelie, C. Champeaux, and A. Catherinot, "Study by a Monte Carlo simulation of the influence of a background gas on the expansion dynamics of a laser-induced plasma plume," Applied Physics A **69**, 45-50 (1999).
17. T. Zhou, S. Kraft, W. Perrie, J. Schille, U. Löschner, S. Edwardson, and G. Dearden, "Backward Flux Re-Deposition Patterns during Multi-Spot Laser Ablation of Stainless Steel with Picosecond and Femtosecond Pulses in Air," Materials **14**, 2243 (2021).
18. J. S. Diaz, and S. E. Rigby, "Blast wave kinematics: theory, experiments, and applications," Shock Waves **32**, 405-415 (2022).
19. J. Schille, L. Schneider, A. Streek, S. Kloetzer, and U. Loeschner, "High-throughput machining using a high-average power ultrashort pulse laser and high-speed polygon scanner," Optical Engineering **55**, 096109 (2016).
20. J. Leach, G. Sinclair, P. Jordan, J. Courtial, M. J. Padgett, J. Cooper, and Z. J. Laczik, "3D manipulation of particles into crystal structures using holographic optical tweezers," Optics Express **12**, 220-226 (2004).
21. S. Chang, and C. Grover, "Engineering implementation of a hybrid optical correlator using SLMs," Optics and lasers in engineering **42**, 263-275 (2004).
22. Z. Jiang, K. Takayama, K. Moosad, O. Onodera, and M. Sun, "Numerical and experimental study of a micro-blast wave generated by pulsed-laser beam focusing," Shock waves **8**, 337-349 (1998).
23. A. Chemin, M. W. Fawaz, and D. Amans, "Investigation of the blast pressure following laser ablation at a solid–fluid interface using shock waves dynamics in air and in water," Applied Surface Science **574**, 151592 (2022).
24. G. I. Taylor, "The formation of a blast wave by a very intense explosion I. Theoretical discussion," Proceedings of the Royal Society of London. Series A. Mathematical and Physical Sciences **201**, 159-174 (1950).
25. S.-B. Wen, X. Mao, R. Greif, and R. E. Russo, "Laser ablation induced vapor plume expansion into a background gas. II. Experimental analysis," Journal of applied physics **101**, 023115 (2007).
26. E. J. Kautz, A. Zelenyuk, B. Gwalani, M. J. Olszta, M. C. Phillips, M. J. Manard, C. W. Kimblin, and S. S. Harilal, "Impact of environmental oxygen on nanoparticle formation and agglomeration in aluminum laser ablation plumes," The Journal of Chemical Physics **159** (2023).
27. W. Deal, "Shock Hugoniot of air," Journal of Applied Physics **28**, 782-784 (1957).
28. M. Van Dyke, and A. Guttmann, "The converging shock wave from a spherical or cylindrical piston," Journal of Fluid Mechanics **120**, 451-462 (1982).
29. K. Takayama, H. Kleine, and H. Grönig, "An experimental investigation of the stability of converging cylindrical shock waves in air," Experiments in Fluids **5**, 315-322 (1987).
30. S. Qiu, and V. Eliasson, "Interaction and coalescence of multiple simultaneous and non-simultaneous blast waves," Shock Waves **26**, 287-297 (2016).
31. S. Betelu, and D. Aronson, "Focusing of noncircular self-similar shock waves," Physical Review Letters **87**, 074501 (2001).
32. M. Vreugdenhil, D. Van Oosten, and J. Hernandez-Rueda, "Dynamics of femtosecond laser-induced shockwaves at a water/air interface using multiple excitation beams," Optics letters **43**, 4899-4902 (2018).
33. D. Baasanjav, J. Hernandez-Rueda, A. P. Mosk, and D. Van Oosten, "Optical method for micrometer-scale tracerless visualization of ultrafast laser induced gas flow at a water/air interface," Applied Optics **59**, 5205-5209 (2020).
34. A. Pereira, P. Delaporte, M. Sentis, A. Cros, W. Marine, A. Basillais, A. Thomann, C. Leborgne, N. Semmar, and P. Andreazza, "Laser treatment of a steel surface in ambient air," Thin Solid Films **453**, 16-21 (2004).
35. M. M. Peri, I. Varghese, and C. Cetinkaya, "Laser cleaning for removal of nano/micro-scale particles and film contamination," in *Developments in Surface Contamination and Cleaning*(Elsevier, 2011), pp. 63-122.
36. R. Klemens, P. Oleszczak, and P. Zydak, "Experimental and numerical investigation into the dynamics of dust lifting up from the layer behind the propagating shock wave," Shock Waves **23**, 263-270 (2013).
37. A. Radhakrishnan, J. Gateau, P. Vlugter, and Y. Bellouard, "Femtosecond laser-shockwave induced densification in fused silica," arXiv preprint arXiv:2202.13580 (2022).
38. J. Dewey, D. McMillin, and D. Classen, "Photogrammetry of spherical shocks reflected from real and ideal surfaces," Journal of Fluid Mechanics **81**, 701-717 (1977).

Acknowledgments: We would like to thank Professor John Costello (FRS), Dublin City University for his valuable discussions and encouragement regarding this work. We also thank Professor Miles Padgett, the University of Glasgow for use of CGH generating software in Labview. We gratefully acknowledge access to the SEM Shared Research Facility at the University of Liverpool. **Funding:** The authors declare no funding based on this work. **Author contributions:** T.Z., W.P. and G.D. designed the experiments; T.Z., S.K. and Z.F carried out the experiments; T.Z., S.K. Z.F. and M.B. contributed to SEM measurements while M.B. provided EDX spectra. T.Z. performed the simulations, T.Z. and W.P conducted theoretical calculations; T.Z., W.P., S.K., Z.F. S.E. and M.B. analysed the data; G.D., S.E., J.S. and U.L. supervised the project. All authors contributed to the preparation of the manuscript. **Competing interests:** The authors declare no conflict of interest. **Data and materials availability:** All data needed to evaluate the conclusions in the paper are present in the paper and/or the Supplementary Materials.